Advances in Industrial and Manufacturing Engineering 10 (2025) 100161

Contents lists available at ScienceDirect

Advances in Industrial and Manufacturing Engineering

journal homepage: www.sciencedirect.com/journal/advances-in-industrial-and-manufacturing-engineering

Manipulating martensitic transformation and residual stress development in stress superposed incremental forming of SS304

Elizabeth M. Mamros [a], Fabian Maaß [b], Thomas H. Gnäupel-Herold [c], A. Erman Tekkaya [b,*], Brad L. Kinsey [d], Jinjin Ha [d]

[a] Department of Mechanical Engineering, Bucknell University, Lewisburg, PA, 17837, USA
[b] Institute of Forming Technology and Lightweight Components, TU Dortmund University, 44227, Dortmund, Germany
[c] Neutron-Condensed Matter Science Group, National Institute of Standards and Technology, Gaithersburg, MD, 20899, USA
[d] Department of Mechanical Engineering, University of New Hampshire, Durham, NH, 03824, USA

ARTICLE INFO

Keywords:
Stainless steel
Stress superposition
Incremental forming
Martensite transformation
Residual stresses

ABSTRACT

Stress superposition is one of the strategies used in metal deformation processes to increase the material formability, decrease the required forming forces, and create highly customized components. To investigate the effects of tensile and compressive stresses superposed to the single point incremental forming (SPIF) process, experiments and numerical simulations were conducted for a stainless steel 304 (SS304) truncated square pyramid geometry. Tensile stresses were superposed in-plane on the specimen blank by a custom hydraulic frame, and compressive stresses were incorporated via a polyurethane die. Identified parameters for a martensitic transformation kinetics model for SS304 were used in a two-step finite element approach to predict the α'-martensite volume fraction. These results were compared to experimental results measured by a Feritscope at four locations along each pyramid wall and validated by electron backscatter diffraction. The residual stresses were measured using x-ray diffraction. The parts from each incremental forming process revealed differences in the residual stresses, which impacted the final geometries, and the α'-martensite volume fraction at the four measurement locations. The evolution of the stress state, defined by the stress triaxiality and Lode angle parameter, for each process contributed to the phase transformation variance. It was found that superposing both tensile and compressive stresses to SPIF resulted in the greatest phase transformation and lowest magnitude of residual stresses near the base and the greatest overall geometrical accuracy. Stress-superposed incremental forming can be implemented to manipulate final part properties, which is ideal for applications requiring highly customized parts, e.g., biomedical trauma fixation hardware.

1. Introduction

For creating the highly customizable components required in various industries, e.g., trauma fixation hardware in the biomedical industry (Lu et al., 2016), flexible manufacturing processes are desired. Incremental forming is one example of a rapid prototyping process that can achieve this objective without the use of custom tooling. The conventional single point incremental forming (SPIF) process simply requires a milling machine, hemispherical tool, and support frame for the blank to implement in an industrial environment (Duflou et al., 2018). During SPIF, a user-defined toolpath guides the tool in a layer-by-layer manner to impose local deformation until the desired geometry is achieved (Kalpakjian and Schmid, 2013). This process is ideal for thin sheets and materials such as metals and polymers. Incremental forming is a combination of bending, tension, and shear deformation mechanisms (Martins et al., 2008). Their individual contributions to the deformation can be varied to impact the residual stresses in the final part as shown for a groove geometry in (Maaβ et al., 2019).

One of the emerging strategies used in manufacturing to increase material formability, decrease the required forming loads, and enable customization of components is stress superposition (Tekkaya et al., 2023). Stress superposition is defined as the introduction of additional stresses into a single processing step. One example is incremental tube forming, which involves applying bending and spinning to a tube simultaneously (Becker et al., 2014). This stress-superposed process enables curved geometries to be manufactured from high strength

* Corresponding author.
E-mail address: erman.tekkaya@iul.tu-dortmund.de (A.E. Tekkaya).

https://doi.org/10.1016/j.aime.2025.100161
Received 9 December 2024; Received in revised form 4 March 2025; Accepted 17 March 2025
Available online 18 March 2025

materials with decreased bending moments. Another example is the continuous bending under tension (CBT) process, which superposes bending via a set of rollers to a specimen in uniaxial tension and has been likened to the SPIF process (Emmens and van den Boogaard, 2009). While not referred to as stress superposition in their work, Bochniak and Korbel incorporated cyclic torsion into several processes, e.g., extrusion (Bochniak and Korbel, 2000), forging (Bochniak and Korbel, 2003), and thin-walled tube drawing (Bochniak et al., 2005), which achieve forming improvements, as well as rolling with shear to refine the grain structure (Korbel and Bochniak, 2004).

Alternatively, the stress superposition strategy can be adopted to manufacture functionally graded parts using stress state sensitive microstructure changes, e.g., martensite transformation (Mamros et al., 2024), twinning/detwinning, texture, etc., of metallic materials. These heterogeneous parts are advantageous for applications requiring highly customized parts, such as biomedical trauma fixation hardware, which are implants to fixture fractured bones together during healing (Pompe et al., 2003). Prior to the implementation of stress-superposed incremental forming (SSIF) variants on the conventional SPIF process, one investigation concluded that the most effective method of controlling the martensitic phase transformation during SPIF was by adjusting the process temperature (Katajarinne et al., 2014). More recently, SSIF variants such as tensile (TSSIF) and compressive (CSSIF) have been proposed. For instance, a polyurethane die was introduced when forming aluminum alloy 5083 to superpose compressive stresses into the SPIF process, so-called compressive stress superposed incremental forming (CSSIF), which affected the residual stress development (Maaβ et al., 2021). Another variant, hydro-assisted incremental forming uses fluid hydrostatic pressure to affect the stress state and was studied for a low carbon steel in (Fatemi and Mollaei Dariani, 2024). For tensile stress superposed incremental forming (TSSIF), investigations have examined the effect on residual stresses (Maaβ et al., 2022) and phase transformation (Mamros et al., 2022). Note that the phase transformation behavior of the material can be directly influenced by manipulating the stress state or other parameters, including the temperature in the forming zone, strain rate, and equivalent plastic strain level (Feng et al., 2021), during manufacturing processes. The stress path can also affect the phase transformation, which was demonstrated for SS304 subjected to double-sided incremental forming (DSIF), e.g., by varying the deformation path (Darzi et al., 2023), by inducing reverse loading with a reforming path (Darzi et al., 2024a), and with a localized reforming path (Darzi et al., 2024b). Due to the superposition of compressive stresses generated through the sheet thickness between the forming and support tools to SPIF, DSIF is another example of a stress-superposed process, including tension, bending, shear, and compression deformation mechanisms (Moser, 2019).

To further investigate the effects of stress superposition on incremental forming, researchers have proposed that simplified stress superposed processes can be considered. For example, the continuous bending under tension (CBT) process was used by Emmens and van den Boogaard (Emmens and van den Boogaard, 2009) and Poulin et al. (2020) to experimentally investigate how parameters, such as the pulling speed and depth setting, affect the amount of total elongation to fracture. Ha et al. analyzed the enhanced total elongation of CBT, compared to simple uniaxial tension, in relation to the influence of texture attributes (Ha et al., 2022), and Mayer et al. (2024) demonstrated the recovery of ductility after CBT at the expense of strength through the annealing process. More recently, Mamros et al. performed CBT experiments to study the effects of strain level and temperature on the phase transformation and residual stress development of SS304 in a bending-tensile stress superposed process (Mamros et al., 2023). Peng and Ou used CBT and CBT with simultaneous compression, so-called tension under cyclic bending and compression, via the addition of a fourth roller, to evaluate the deformation mechanisms in SPIF and DSIF, respectively (Peng and Ou, 2023).

In this work, SPIF and three stress-superposed incremental forming (SSIF) variants, TSSIF, CSSIF, and tensile compressive stress-superposed incremental forming (TCSSIF), were investigated experimentally and numerically. This is the first publication to the author's knowledge that investigates TCSSIF and the first to compare these three stress superposed variants to one another and to SPIF. The primary objective was to determine the effect of the different stress states during deformation on the properties, e.g., the geometry, phase transformation, and residual stresses, of the final product, i.e., a truncated square pyramid for this investigation. Section 2 summarizes the material characterization for SS304. Section 3 details the constitutive modeling for SS304 and polyurethane 90° shore A. An isotropic, combined strain hardening law for constituent phases was identified to model SS304 and coupled with the Beese and Mohr (2011) martensitic transformation kinetics model (Beese and Mohr, 2011). Section 4 describes the incremental forming experiments, including the experimental setup and process variants. Section 5 overviews the numerical modeling in Abaqus (2019); Hibbitt et al. (1978) for each process using a two-step approach (Mamros et al., 2024). First, explicit simulations for each IF process were completed without phase transformation kinetics. In the second step, the nodal displacements from select elements in the full process models were used as the boundary conditions for one element simulations coupled with a user material (UMAT) subroutine for implicit simulations to predict martensitic transformation. Section 6 presents the results and discussion. The numerical results were validated by experimental results for all four IF processes. A Feritscope was used to measure the α'-martensite volume fraction on the formed parts and validated by electron backscatter diffraction (EBSD) measurements. The residual stresses along the rolling direction (RD) were analyzed by x-ray diffraction (XRD), and a microetching procedure was used to evaluate the through-thickness residual stress gradient. Section 7 includes the conclusions and possible topics for future work. Collectively, the results obtained here support that stress superposition can be used strategically in incremental forming to customize product properties and achieve functionally graded parts for specific applications, e.g., biomedical trauma fixation hardware described in (Cheng et al., 2020).

2. Material characterization

SS304 sheets with an initial thickness of 0.8 mm were characterized by uniaxial tension, bulge, in-plane torsion, and disk compression experiments. The resulting α'-martensite volume fractions were measured using an FMP30 Feritscope (Fischer Technology Inc.) and validated by electron backscatter diffraction (EBSD). The uniaxial tension experiments followed the specimen geometry specified by the ASTM E8 standard (ASTM International, 2024) and the displacement rates specified by ISO 6892-1 (ISO 6892-1:2019, 2019). The bulge test experiments followed the DIN 51524-2 standard (DIN 51524-2, 2017). Further details regarding the material characterization experiments can be found in (Mamros et al., 2024). The chemical composition provided by the supplier is shown in Table 1. The Young's Modulus is approximately 170 GPa calculated from the stress-strain curve of uniaxial tension in the RD, and the Poisson's ratio is 0.33 based on the textbook value (Kalpakjian and Schmid, 2013).

The initial texture was determined by EBSD using a Tescan Lyra3 focused ion beam scanning electron microscope (FIB-SEM) with an EDAX Pegasus EBSD system. A beam intensity of 19.1 and an acceleration voltage of 20 kV were used, and the measurement area was approximately 495 μm along RD and 380 μm along the transverse direction (TD)/normal direction (ND). The Feritscope measurements on ferrite volume fraction for the as-received material were <0.01

Table 1
Supplier provided chemical composition of stainless steel 304.

% C	% Si	% Mn	% P	% S	% Cr	% Ni	% Fe
0.07	1.00	2.00	0.045	0.030	17.00–19.5	8.50–10.50	Bal.

α'-martensite before and after polishing. Note that the grinding and polishing preparation procedure for the EBSD sample pucks induced additional phase transformation on the surface prior to scanning. Since EBSD is a localized measurement with a small penetration depth (typically 10 nm–40 nm at 20 kV (Dingley, 2004)), the sample preparation inflates the α'-martensite volume fraction for EBSD compared to the volumetric measurement of the Feritscope where the measurement region was circular at the surface (radius 3 mm) with a depth penetration <1 mm ("Data Sheet for the Probes FGAB1.3-Fe and EGAB1.3-Fe," n.d.). Due to attenuation, the Feritscope measurements are weighted toward the surface layer. This is consistent with past research results on martensitic transformation due to deformation of the surface layer after mechanical polishing (Ambrož et al., 2020). The as-received material is assumed to be fully austenitic, which indicates a face centered cubic (FCC) crystal structure. The pole figures describing the initial material texture are shown in Fig. 1. The {111} texture observed is consistent with a rolled sheet material.

3. Constitutive modeling

3.1. SS304 stainless steel

The SS304 material behavior, including phase transformation, was assumed to be isotropic for simplicity in modeling. The key aspects of the constitutive model used in this work are summarized in this section (Table 2), but additional details can be found in (Mamros et al., 2024). The pertinent equations and parameters are summarized in Table 2.

Swift strain hardening models were used to describe the behavior of the constituent phases, i.e., γ-austenite and α'-martensite, individually. Then, these true stress-strain curves were combined in a weighted equivalent stress equation, which is a function of the phase volume fraction, i.e., the α'-martensite volume fraction denoted by $f_{\alpha'}$. A similar approach to modeling the strain hardening of an austenitic stainless steel was used in (Luo and Yuan, 2022).

The martensitic transformation kinetics was described using the isotropic Beese and Mohr (2011) model (Beese and Mohr, 2011), which was modified from the Santacreu et al., (2006) model (Santacreu et al., 2006). Initially, Stringfellow et al. (1992) expanded the Olson and Cohen (1975) model (Olson and Cohen, 1975) to incorporate the stress state via the stress triaxiality, η. Based on experimental observations, Beese and Mohr expanded the definition of the stress state to include the Lode angle parameter, $\bar{\theta}$. Consistent with the Santacreu et al., (2006) model (Santacreu et al., 2006), this model assumes isothermal conditions, and the maximum achievable volume fraction, $c_{\max}$, is dictated by the temperature value. In (Santacreu et al., 2006), the maximum transformation for SS304 at 20 °C was determined through experiments to be ~0.5, which is comparable to the value determined in this work. The experimental data and α'-martensite volume fractions predicted by this model for uniaxial tension, uniaxial compression, shear (in-plane torsion), and equibiaxial tension (bulge test) are explained further and shown in (Mamros et al., 2024). The transformation kinetics order from greatest to least with respect to equivalent plastic strain for SS304 is as follows: shear, equibiaxial tension, uniaxial tension, and uniaxial compression. Note that this order is dependent on the specific SS material and component form investigated (Tekkaya et al., 2023).

Table 2
Summary of SS304 isotropic strain hardening and martensitic transformation kinetics modeling. $\bar{\sigma}$ and $\bar{\varepsilon}$ are the phase averaged stress and strain; K, b and ε_0 are material specific parameters.

Strain hardening model		$\bar{\sigma} = f_{\alpha'} \bullet \sigma_{\alpha'} + (1 - f_{\alpha'}) \bullet \sigma_{\gamma}$		
Swift model		$\sigma = K(\varepsilon_0 + \bar{\varepsilon})^b$		
	K (MPa)	ε_0	b	
$\sigma_{\alpha'}$	1547	0.002	0.11	
σ_{γ}	1313	0.050	0.36	
Martensitic transformation model		$\dot{c} = (c_{\max} - c) n D (D\bar{\varepsilon})^{n-1} \dot{\bar{\varepsilon}}$		
		$D = D(\eta, \bar{\theta}) = (D_0 + a_\theta \bar{\theta} + a_\eta \eta)_+$		
$c_{\max}$	n	D_0	a_θ	a_η
0.49	2.13	2.05	0.10	0.46

3.2. Polyurethane (PU) 90° shore A

Polyurethane (PU) 90° Shore A was chosen for the die material. To characterize this material, cyclic compression experiments were conducted according to ISO 7743 (ISO 7743:2017, 2017). In each experiment, a cylindrical specimen with an initial height of 30 mm and initial diameter of 20.5 mm was subjected to three compressive cycles. Three repetitions were conducted to ensure consistency of the results. The resulting force-displacement curve from a representative experiment is shown in Fig. 2.

For the polyurethane die, a hyperelastic material model was used, which derives the stress-strain relation from the deformation energy density. According to the Mooney-Rivlin model (Mooney, 1940), the dependence of the strain energy density (MJ/m^3) on the deformation is expressed by a polynomial equation with the strain invariants of the Cauchy-Green strain tensor, I_1 and I_2, (Stommel et al., 2018):

$$W = \sum_{i+j=1}^{N} C_{ij} \bullet (I_1 - 3)^i (I_2 - 3)^j \quad (1)$$

For $N = 1$, the Mooney-Rivlin model reduces to the two-parameter form. The parameters C_{10} and C_{01} required for the simulation were calculated using Abaqus from the experimental data of the cyclic compression tests. Their values were $C_{10} = 1.714$ MPa and $C_{01} = -0.186$ MPa.

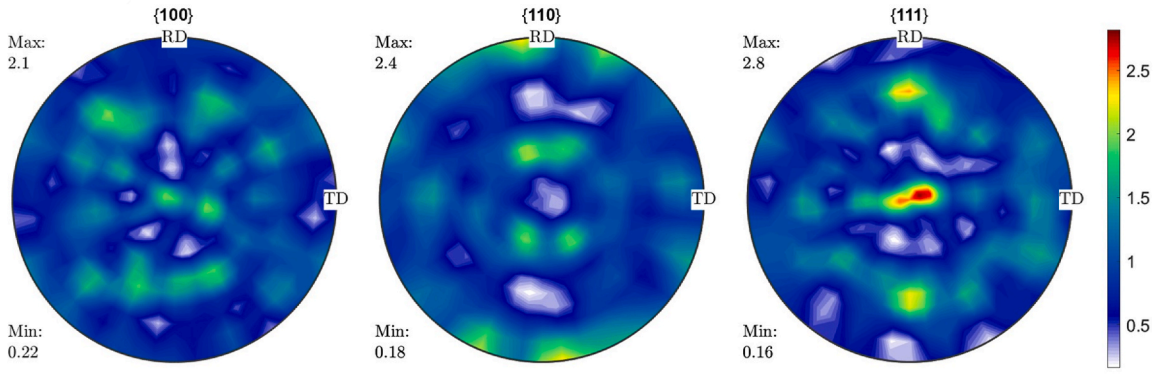

Fig. 1. Pole figures for initial texture of SS304 as-received material (FCC).

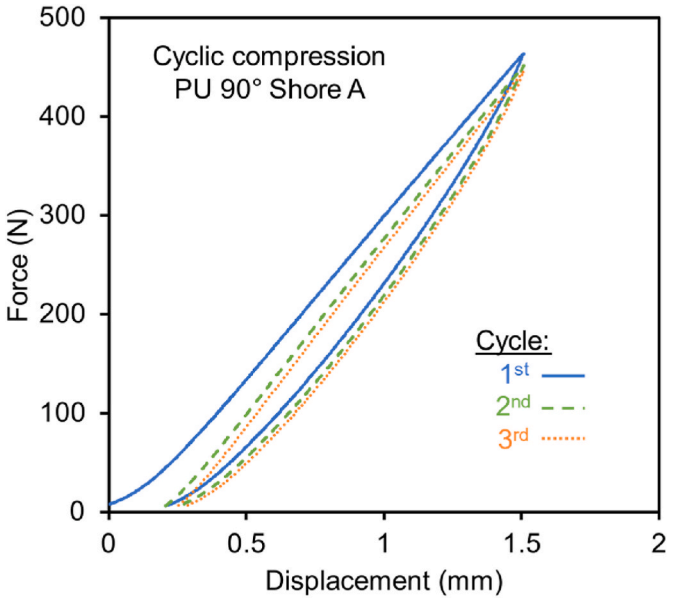

Fig. 2. Force-displacement curve for cyclic compression of polyurethane (PU) 90° Shore A.

4. Incremental forming experiments

The conventional incremental forming process, SPIF, and three variants with stress superposition, TSSIF, CSSIF, and TCSSIF were investigated. For consistency purposes, the same toolpath and general experimental setup were used for all four forming processes. Details regarding the SPIF setup, specimen blank, target geometry, and forming tool are given in Section 4.1, including parameters measured during and after the experiments. The additions of tensile and compressive stresses are detailed in Sections 4.2 and 4.3, respectively.

4.1. Overview and setup

The specimens were laser cut from SS304 sheets of 0.8 mm thickness into the shape shown in Fig. 3. The forming area remained square while the arms contained holes for the bolts to pass through in the grips, which were necessary for the experiments where tension was applied to the sheets. The bottom surface of each specimen, i.e., non-toolside, was electrochemically etched with a dot pattern to allow for strain and geometry measurements via a photogrammetry camera after forming. An 85 mm base truncated square pyramid with a 45° wall angle was the target geometry and is shown in Fig. 3.

The incremental forming experiments were conducted using a 5-axis DMU50 milling machine (DMG Mori). The machine's computer numerical controller was programmed to follow a user-defined,

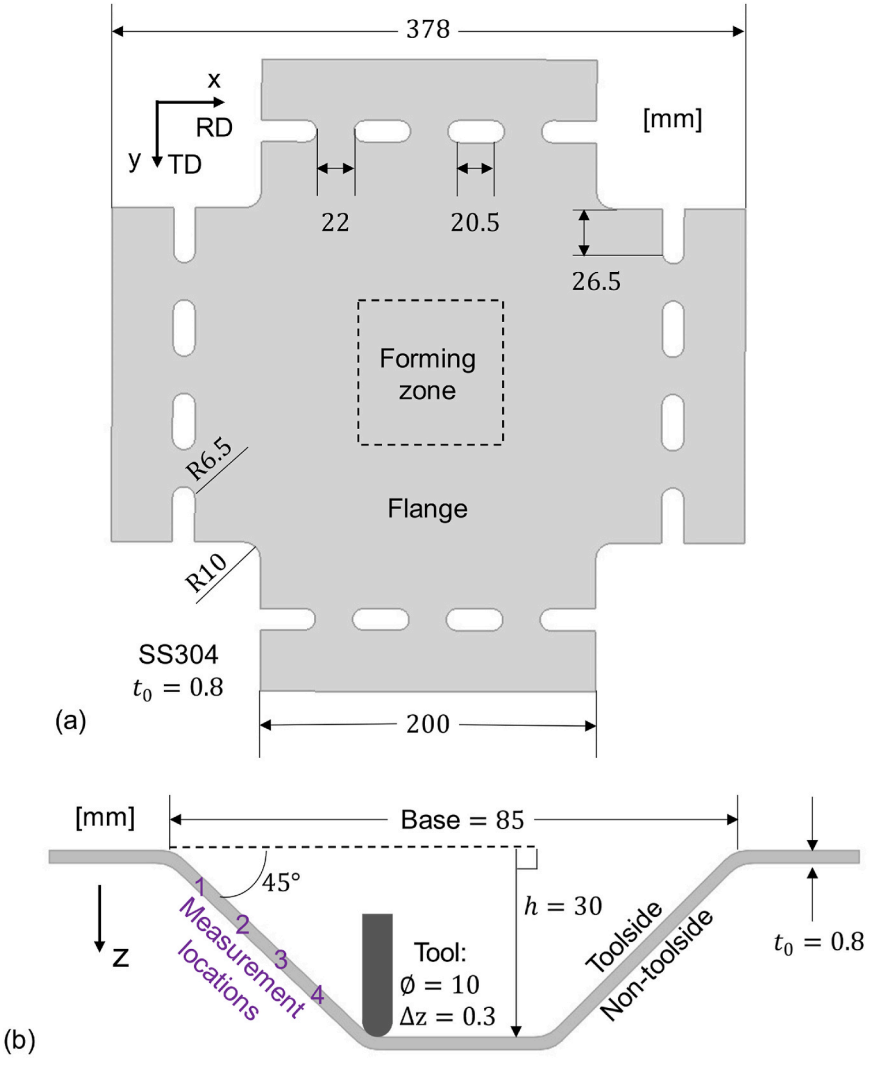

Fig. 3. Incremental forming (a) blank, (b) target, and forming tool geometries.

bidirectional toolpath, programmed in MATLAB (MathWorks), and the start point for each layer was located at the corner farthest from the two cylinders of the frame as indicated in Fig. 4a. For all process variants, a fixed (spindle rotation = 0 rpm), hemispherical tool with a 10 mm diameter tip was used with a step down of 0.3 mm and constant feed rate of 1500 mm/min, which resulted in a total forming time of approximately 811 s for the 30 mm depth. The base of the square truncated pyramid was formed first, i.e., an outside-in strategy was employed. A thin layer of deep-drawing oil ("Castrol Iloform PN 226 Datasheet," 2008) was applied to the surface of the sheet prior to each experiment. A custom hydraulic frame was installed to act as a blankholder (Fig. 4), and during SPIF, a minimal pressure (<5 bar) was applied to the hydraulic cylinders to fix the sheet specimens in-plane at the initial gripped position. The sheet blank was aligned such that the RD coincided with the x-axis of the setup.

For each of the IF experiments, the axial force and temperature were recorded during forming. After removing the formed parts from the blankholder, the geometry and residual stresses were analyzed. Additionally, the phase transformation was measured using a nondestructive technique, a Feritscope, and validated by EBSD. More details regarding these methodologies and analyses can be found in their respective subsequent sections.

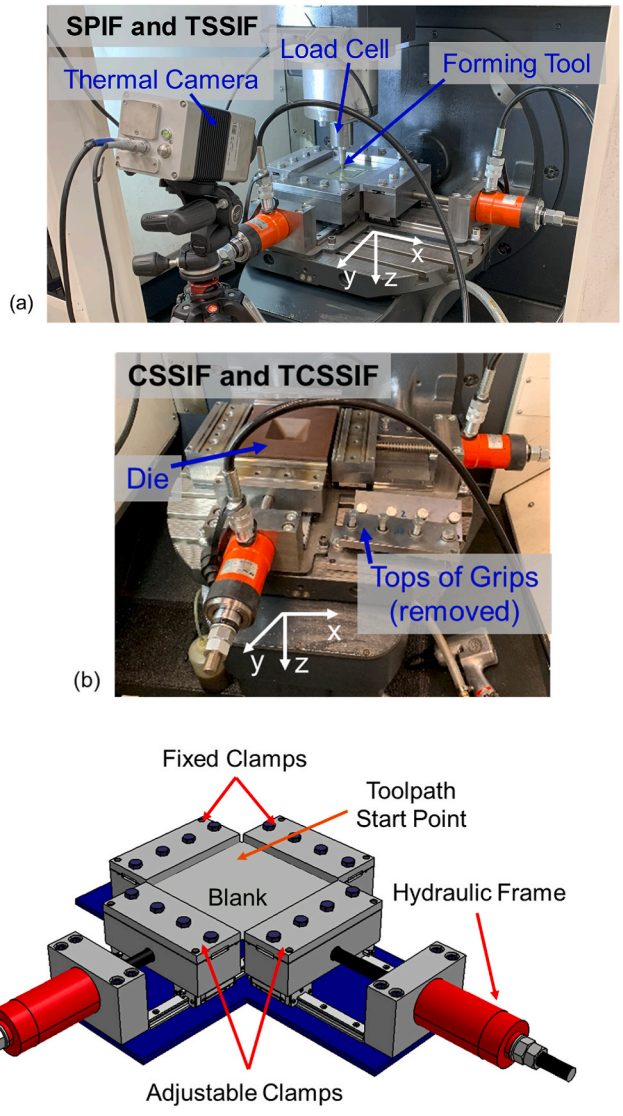

Fig. 4. Experimental setup inside DMU 50 for (a) SPIF and TSSIF; and with die added for (b) CSSIF and TCSSIF processes; and (c) schematic of custom frame.

4.2. Tensile stress-superposition

The hydraulic frame shown in Fig. 4 was used to superpose equibiaxial tensile stress to the SPIF process for two SSIF variants: TSSIF and TCSSIF. For both cases, the frame was set to its maximum pressure, i.e., ~200 bar for each cylinder, to apply in-plane equibiaxial tension to the sheet metal blank. Digital Image Correlation (DIC) measured that the von Mises strain (equivalent strain by von Mises yield function) achieved across the forming area is ~0.01. This includes the elastic strain component.

4.3. Compressive stress-superposition

To superpose compressive stress to the SPIF process, a polyurethane die (190 mm × 190 mm x 50 mm) was used in conjunction with the experimental setup described previously to form two SSIF variants: CSSIF and TCSSIF. A riser is placed in the center of the forming section in the tensile frame and holds the die securely (Fig. 4b). The negative die cavity was milled into the surface of the die to the target geometry dimensions. Thus, a compressive phenomenon, so-called squeeze factor in DSIF, proportional to the sheet thickness, was applied at the tool contact point with the sheet during forming. A thin layer of the same lubricant described in Section 4.1 was also applied to the surface of the die cavity between experiments. Note that the die and die riser were removed from the experimental setup for SPIF and TSSIF experiments.

5. Numerical modeling

An overview of the numerical model created for the SPIF process is described in Section 5.1 and detailed further in (Maaβ et al., 2022). The SPIF FE model is used and modified as necessary for the SSIF process variants. For TSSIF and TCSSIF, an additional simulation step was required to model the tensile stress superposition (Section 5.2). For CSSIF and TCSSIF, another component was required in the model assembly to represent the polyurethane die (Section 5.3). A two-step approach was used: 1) a full incremental forming process simulation using Abaqus/Explicit 2019 with only isotropic elastic-plastic models, i.e., Hooke's law combined with von Mises yield function and Swift strain hardening, not considering phase transformation, to determine the strain in a given element at a specified location; 2) one element simulations using Abaqus/Implicit 2019 with isotropic elastic-plastic models with martensite transformation kinetics, which were implemented into a user material subroutine (UMAT), to predict the martensitic transformation at select locations (Section 5.4). Note that this was not a thermal-mechanical analysis.

5.1. Model overview

The SPIF process was modeled using linear brick elements with reduced integration, C3D8R, for the sheet with three elements through the sheet thickness direction. Note that a simplified sheet geometry was used in the model that excluded part of the gripped region and the corresponding holes. A subsection of the forming area that is larger than the target geometry contained a refined mesh for increased accuracy. A transition zone is partitioned around this subsection, and the remaining flange area was coarsely meshed to increase computational efficiency (Fig. 5). Mass scaling of 10^3 was used. The tool was modeled as a rigid body, which neglects the tool deflection used in (Moser et al., 2021). The toolpath used for experiments was converted from lines and coordinates in G-code to amplitudes and step times based on the length of each toolpath layer. This converted toolpath was implemented as displacement boundary conditions without time scaling. Using the same experimental setup, the same lubricant, and rolled sheet specimens, it was determined through strip tension tests that the friction coefficient between the well-lubricated forming tool and the sheet was relatively small ($\mu = 0.03$) (Maaβ et al., 2020a); thus, friction between the tool and

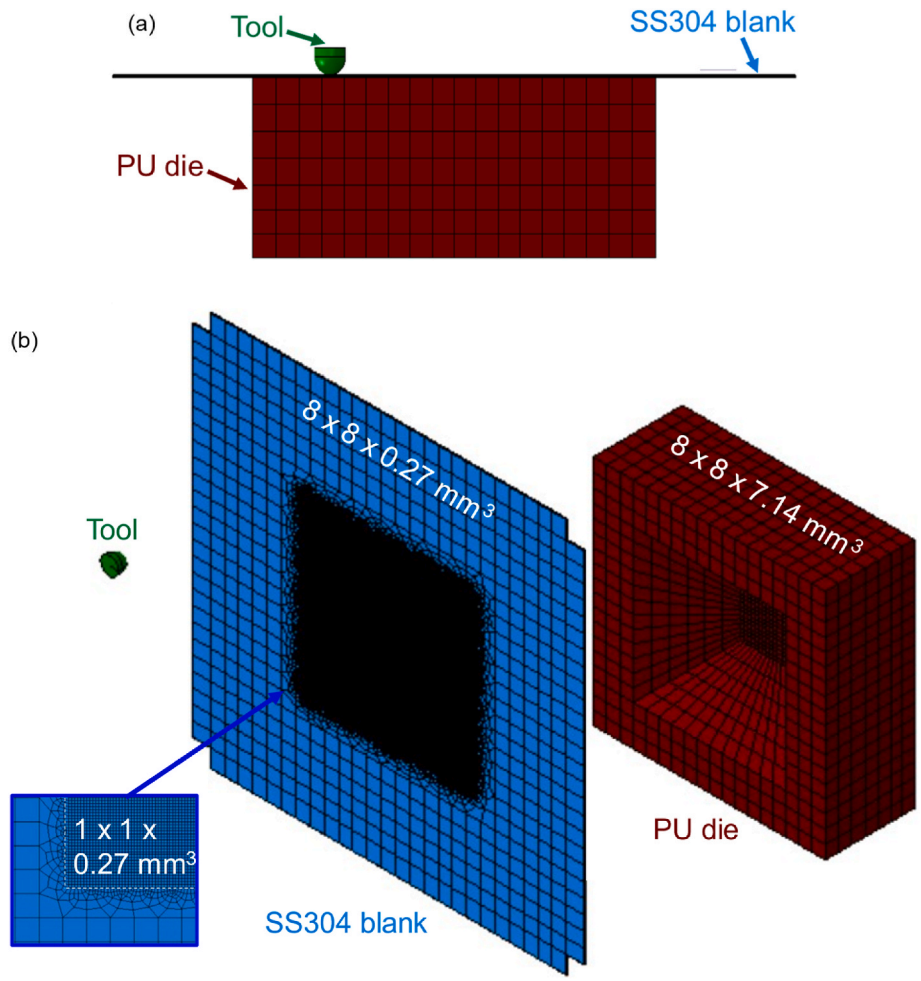

Fig. 5. FE model assembly for CSSIF and TCSSIF: (a) side and (b) exploded isometric views.

the sheet on the toolside and between the sheet and the die on the non-toolside were ignored, i.e., the friction coefficient, $\mu = 0$.

5.2. Tensile pre-stress step

To superpose tensile stress in the numerical model, a step for pre-stress was added to the TSSIF and TCSSIF simulations. During this step, the tool and the clamped, i.e., -x and -y, sides of the blank were fixed. Displacement boundary conditions were applied to the adjustable, i.e., +x and +y, sides of the blank. The displacement value, i.e., 1.975 mm, was chosen to create approximately 1 % von Mises strain in the forming area to replicate the DIC experimental results of the loaded blank in the tensile frame.

5.3. Compressive die component

To superpose the compressive stress in the numerical model, the polyurethane die was included in the assembly as a deformable body. PU 90° Shore A was modeled based on the results in Section 3.2. The die contained 2988 elements (type C3D8R) with seven elements through the thickness and is shown in Fig. 5. The interaction between the die and the sheet was modeled as kinematic contact. An additional boundary condition was applied to impose the displacement restrictions on the riser used in experiments.

5.4. One element simulation for martensitic phase transformation

One element, implicit simulations were used to predict the phase transformation along the pyramid walls at the same locations as the Feritscope measurements. The nodal displacements from 12 elements for each incremental forming variant, i.e., four elements from the toolside, midplane, and non-toolside, from the full model simulations were exported and prescribed as the boundary conditions for the one element simulations. The isotropic strain hardening and martensitic transformation kinetics models were combined in the UMAT to describe the deformation induced phase transformation in the sheet specimens during stress-superposed incremental forming. This two-step method is both computationally efficient and provides information not readily available experimentally, e.g., the volume fractions at the midplane along the thickness direction, which cannot be measured directly using the Feritscope.

6. Results and discussion

The experimental and numerical results are summarized in Section 6. First, the force and temperature for each IF process were compared (Section 6.1). Next, the geometrical accuracy and the residual stresses were assessed (Section 6.2). Additionally, the final strain state (Section 6.3) and the evolution of the stress and strain during forming from numerical analyses (Section 6.4) are discussed. Lastly, the α'-martensite transformation results from the Feritscope, EBSD, and one element simulations are presented in Section 6.5.

6.1. Force and temperature

During forming, the process force, i.e., along the z-direction, was

recorded by a load cell (Kistler) mounted to the spindle and Catman Easy (HBM) software. An infrared (IR) camera (VarioCAM HD head) was used to record the process temperature on the toolside, which was analyzed using IRBIS 3 (InfraTec) software. Note that the maximum temperature recorded by the IR camera is slightly less than the actual maximum temperature, which is located below the forming tool and obscured from the camera's view. One research group is exploring the possibility of using an artificial neural network to predict the actual forming temperature (Jiang et al., 2022).

The experimental results for the process, i.e., axial or z-, force are shown in Fig. 6. Initially, i.e., for process times <100 s, TSSIF and TCSSIF showed the highest force values due to the tensile prestress applied to the specimen. Then, for process times of 200–350 s, similarly, the compressive stress-superposed variants, i.e., CSSIF and TCSSIF required increased forces, which was expected due to the presence of the die in these processes. The die, particularly the flat surface surrounding the cavity, was in contact with the non-toolside of the sheet and added additional support and decreased bending in the flange region during forming. The peaks visible in the force curves were the results of the tool stepdown for each layer of the toolpath. After the initial increase in force for all IF processes while the tool was between locations 1 and 2, the force started to plateau as the tool approached locations 3 and 4, in particular for the cases with the die. In contrast, SPIF showed increasing force throughout the process.

The experimental results for the maximum recorded temperatures during each process are shown in Fig. 7. Initially, the temperature profiles followed the same trend as the force curves, i.e., TCSSIF showed the largest increase, then TSSIF followed by CSSIF, and SPIF had the lowest temperature near location 1. The presence of the die increased the amount of friction in the system since the non-toolside now also experienced contact and greater resistance to bending. When the geometry near location 2 was formed and for the remainder of the process including locations 3 and 4, the temperatures for CSSIF and TCSSIF continued to increase but less so than in TSSIF and SPIF. This was due to the large contact area between the sheet and the die in the compressive SSIF processes, which promoted heat transfer from the blank to the die. Recall that temperature increase inhibits martensitic transformation.

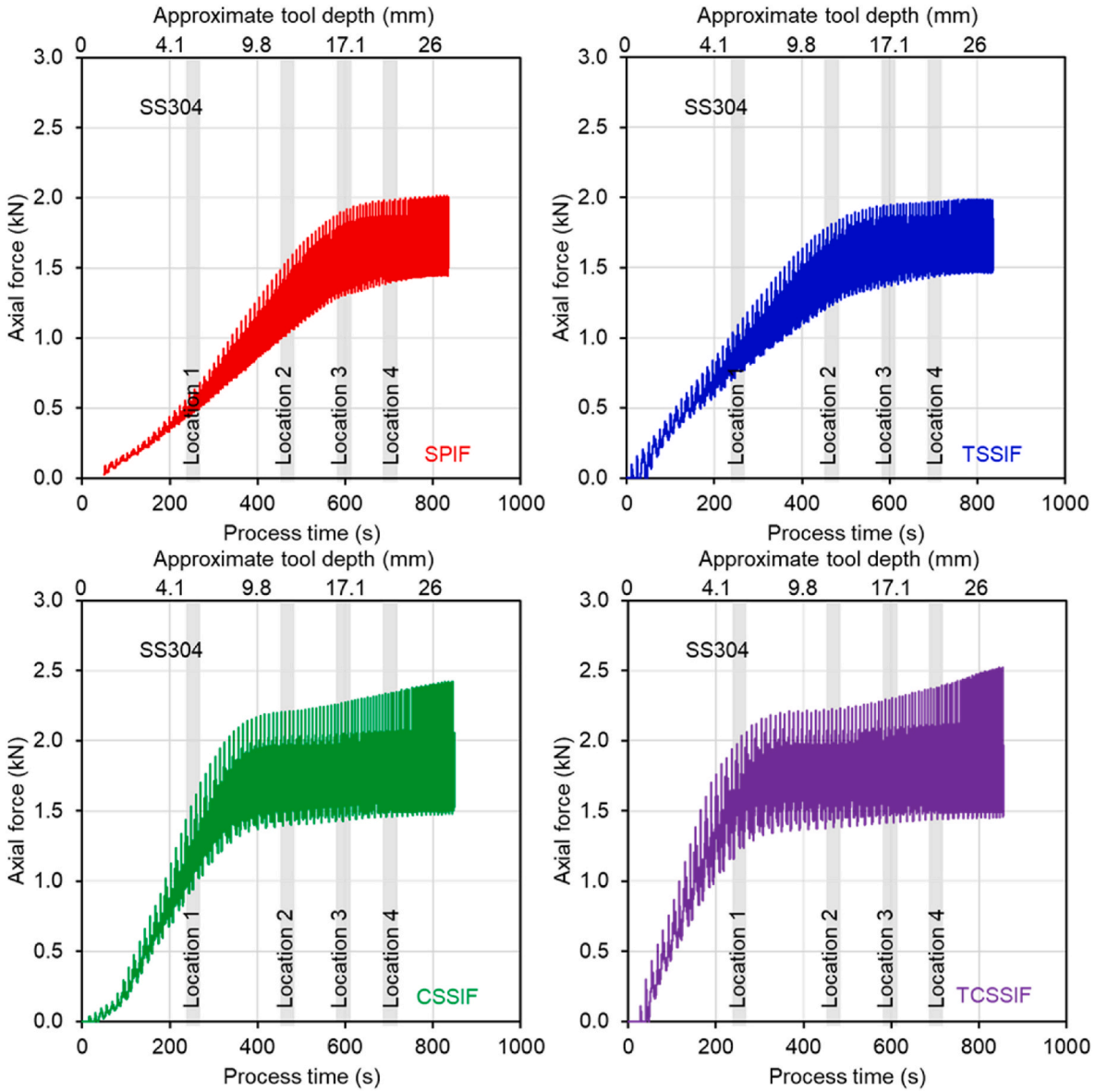

Fig. 6. Axial (z-) force during IF experiments: (a) SPIF, (b) TSSIF, (c) CSSIF, and (d) TCSSIF. The uncertainty of the force signal is 0.2 % (1 × σ).

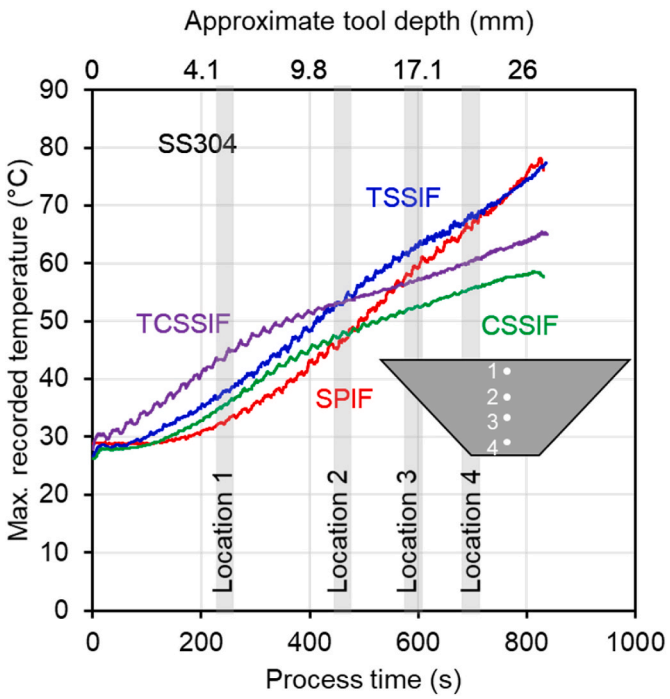

Fig. 7. Maximum recorded temperature during IF processes. The uncertainty of the thermal camera is 40 mK (1 × σ).

6.2. Geometry and residual stress development

After forming, a photogrammetry camera was used to analyze the deformed dot pattern on the non-toolside of the truncated square pyramid in the ARGUS software (GOM). These images were used to determine the profile geometry of the part. Due to the experimental setup, it was not possible to use a DIC system for these experiments to record the strain history, but the final strain state values on the non-toolside were obtained after forming from the images acquired.

The x- and y-profiles along the center of the truncated square pyramid were extracted from the ARGUS models of the formed parts and plotted with the target geometry in Fig. 8. For all process variants, material anisotropy and the experimental setup, i.e., the hydraulic frame, seemed to have negligible effects on the x- and y-profiles, which supports the isotropic modeling assumption used. The truncated surface, i.e., top, of the pyramid was used as the reference for alignment. For consistency, the same toolpath was used for all process variant experiments. However, toolpath optimization could be completed for each process individually to achieve the target geometry. The amount of springback was directly related to the residual stresses developed in the material during forming. TCSSIF had the least amount of springback, i.e., the closest geometry to the target, followed by CSSIF, then TSSIF, and lastly SPIF. Thus, additional investigations into the residual stresses for each process were conducted.

To measure the residual stresses after forming and unclamping the part, XRD was completed at the National Institute of Standards and Technology (NIST) for pyramid wall locations 1–3 on one representative sample from each IF process. Note that location 4 was excluded due to geometrical interference with the measurement equipment. Measurements were obtained for both the toolside and non-toolside using cobalt K-α radiation ($\lambda = 0.17902$ nm) and copper K-α radiation ($\lambda = 0.15418$), respectively. The choice of wavelength was dictated by the requirement of a large diffraction angle to minimize uncertainties. Cobalt K-α radiation was used to measure the (311) austenite reflection and the (310) ferrite/martensite reflection while copper K-α was used to simultaneously measure the pair of austenite (331) and (420) reflections (≈9° difference in diffraction angle) despite the high levels of fluorescent background. However, measurements on the toolside before material removal showed insufficient austenite peak intensity, therefore requiring the use of cobalt K-α radiation for measuring the high angle ferrite (310) reflection. In order to avoid frequent X-ray source changes, it was deemed advantageous to continue using cobalt k-α for measuring austenite (311) after removal of the high-martensite surface layer on the toolside. Data analysis and calculation of X-ray elastic constants was done using IsoDEC (Gnaupel-Herold, 2022; Gnäupel-Herold, 2023).

Additionally, a microetching procedure was used to analyze the residual stress gradient through the thickness of the pyramid wall of a representative CSSIF specimen. A 300 mm custom collimator with 1 mm × 1 mm opening was used to provide sufficiently small beam spots within the etched recesses of approximately 6 mm diameter. Due to the sample shape, it was not possible to perform measurements with a symmetric tilt angle range (both $+\psi$ and $-\psi$); instead, only the negative ψ tilt could be used. Successive microetching for material removal in the thickness direction was performed using a 1:1 solution of concentrated hydrochloric (HCl) and nitric (HNO_3) acids. Each etching step was followed by an x-ray measurement. The etch was applied in a reservoir with 6.4 mm inner diameter glued to the measurement location, i.e., location 2 (see Fig. 9). The removal rate was approximately 3 μm/min; however, faster etching was achieved through frequent exchanges of the

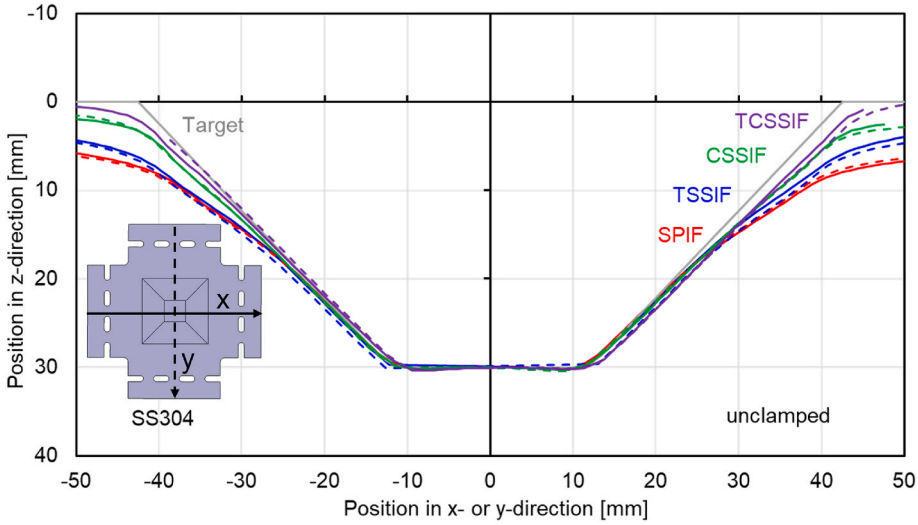

Fig. 8. Comparison of truncated square pyramid cross-sections from IF experiments. Line type indicates cross-section orientation.

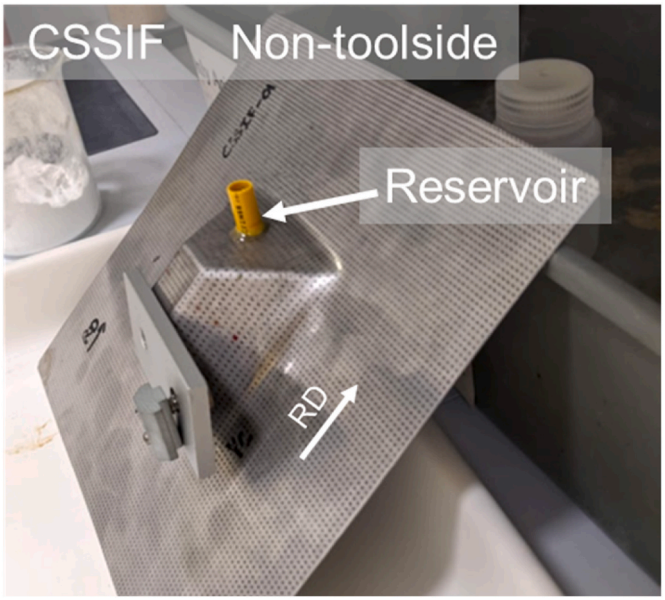

Fig. 9. CSSIF sample with reservoir for microetching prior to XRD attached at location 2 on non-toolside.

etching solution. The depth of the recess was measured through a laser probe (Micro-Epsilon optoNCDT 1320) by scanning the surface profile across the etched region.

In order to limit the effects of material removal on stresses, etching was performed on two opposite walls of the pyramid (see Figs. 9 and 11) for the toolside and non-toolside at location 2. For the toolside etchings, it was found that at depths >0.2 mm (thickness prior to etching was 0.62 mm), the recess started to buckle inward due to the strong compressive residual stresses being relaxed on the non-toolside surface. All residual stresses were measured along the RD.

XRD analyses were used to obtain the residual stresses along the RD direction for the toolside and non-toolside at locations 1 through 3, which are shown in Fig. 10. Measurement uncertainties were estimated from fitting a stress value to the lattice spacings/strains at different tilt angles. The toolside surfaces had unsuitable high-angle reflections for the austenite phase, so the (310) ferrite peak was used instead. Non-toolside measurements presented the reverse problem with very weak intensities for the ferrite peaks; hence, only austenite reflections could be used for stress measurements. On the toolside, the residual stresses for SPIF and TSSIF increased from locations 1 through 3, but for CSSIF and TCSSIF, the residual stresses increased from locations 1 through 2 and then decreased from locations 2 through 3. These trends are related to the effectiveness of the stress superposition mechanism relative to the forming location. Specifically, the tensile superposition effect was most prominent at the beginning of the forming process, i.e., near locations 1 and 2, since the tensile stresses were applied in-plane; however, the compression superposition effect was sustained throughout the forming process since the sheet maintained tangential contact with the die. On the non-toolside, a general trend of increasing compressive residual stresses were observed for locations 1 through 3, except for CSSIF, which showed a slight increase from locations 2 through 3. The relatively large tensile and compressive residual stresses at location 3 are indicative of bending, which led to the wall angle change for $z < 17$ mm in Fig. 8. Correspondingly, this is the location where the formed geometry starts to significantly deviate from the target geometry.

To establish a through-thickness stress profile, spot microetching was performed for the successive removal of surface layers followed by a stress measurement of a CSSIF specimen. The results are shown in Fig. 11. Each removal step led to a re-distribution of stresses. To limit the overall effects on the stresses, non-toolside and toolside etching were

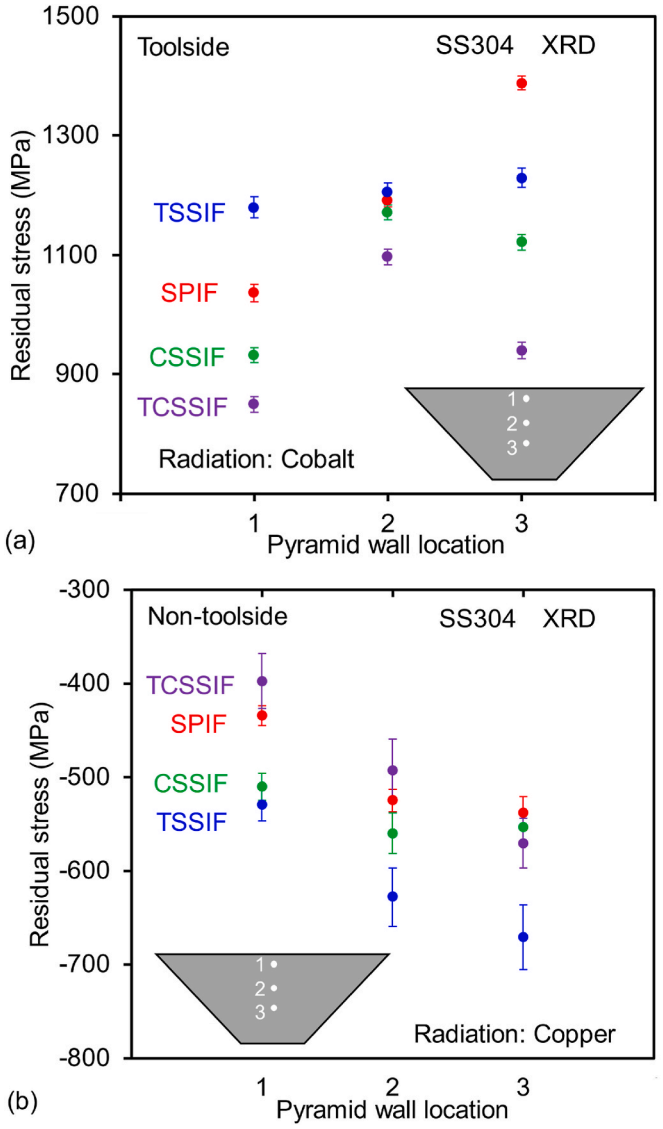

Fig. 10. Residual stresses along RD on (a) toolside and (b) non-toolside from IF experiments at locations 1 through 3 measured by XRD. Error bars represent measurement uncertainty (1 × σ).

performed on two different, opposite sides of the truncated square pyramid as indicated in Fig. 11. The very high magnitude of the compressive stresses on the non-toolside induced buckling in the recessed region when measuring from the toolside; the magnitude of the buckling increased as the remaining 'membrane' became thinner. In particular, the measurements after the third and fourth etching steps, were affected and are circled in Fig. 11.

A correction for buckling was determined analytically by assuming a circular plate with fixed edges (Timoshenko and Woinowsky-Krieger, 1959). First, the pressure applied to the plate to cause the buckling, q, was calculated by:

$$q = \frac{64 \bullet D \bullet w_{\max}}{a^4} \tag{2}$$

where $w_{\max}$ is the maximum deflection from the surface profile measurements, a is the radius of the etched region, and D is the rigidity. The rigidity is defined by:

$$D = \frac{Eh^3}{12(1-\nu^2)} \tag{3}$$

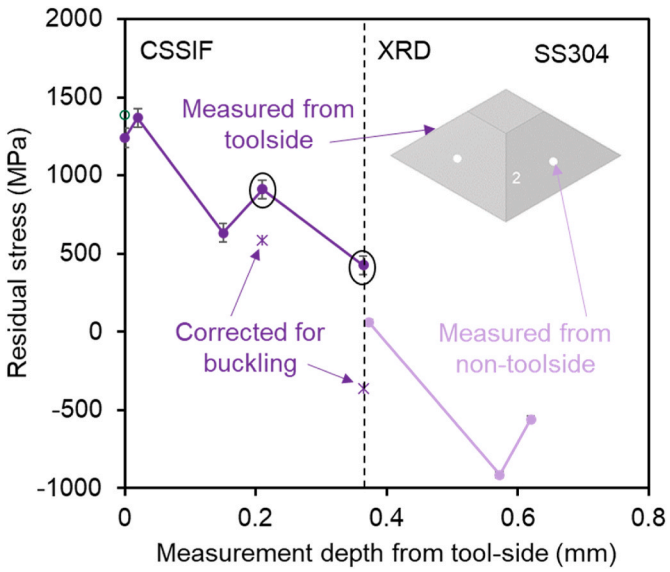

Fig. 11. Residual stresses along RD measured after successive layer removal. Circled data points were affected by buckling. Dashed line represents the depth corresponding to the final measurements. Error bars represent one standard deviation; on the non-toolside error bars are smaller than the size of the symbols.

where E is Young's modulus, h is the material thickness in the recess, and υ is Poisson's ratio. The stress, σ_r, and moment, M_r, along the circumferential sections of the plate are given in Eqs. (4) and (5). From these relations, the average stress over the beam spot size (2.5 mm diameter) due to buckling, $\overline{\sigma_r}$, (Eq. (6)) was derived. Lastly, the buckling stress was subtracted from the measured XRD values. This correction was applied to the affected data points, i.e., at measurement depths of 0.210 mm and 0.364 mm, which correspond to the third and fourth etching steps. The corrected data points are also shown in Fig. 11.

$$\sigma_r = -\frac{6M_r}{h^2} \tag{4}$$

$$M_r = \frac{q}{16}\left[a^2(1+\nu) - r^2(3+\nu)\right] \tag{5}$$

$$\overline{\sigma_r} = \frac{3q}{8\pi h^2 b^2}\left[\frac{a^2b^2}{2}(1+\nu) - \frac{b^4}{4}(3+\nu)\right] \tag{6}$$

Here, a is the recess diameter, b is the diameter of the beam spot, ν is Poisson's ratio, and h is the thickness in the recess.

As seen for SPIF in (Maaβ et al., 2020b), the toolside of CSSIF contains tensile residual stresses while the non-toolside encompasses compressive residual stresses. Prior to etching, the wall thickness near location 2 was 0.62 mm. The lowest residual stresses, i.e., approximately −366 MPa and 60 MPa for the corrected tensile toolside and compressive non-toolside values respectively, were measured near the neutral axis. The dashed line in Fig. 11 represents the depth where the micro-etching procedure was terminated for both pyramid walls and the final measurement was obtained. The mid-thickness of the formed material is located ~0.07 mm to the left of the dashed line in Fig. 11. However, the fourth and fifth toolside measurement points, which are circled in Fig. 11, corresponding to measurements after the third and fourth etching steps, were affected by buckling, which led to increased measured tensile residual stress values. A general decreasing trend is observed from the tensile toolside to the compressive non-toolside of the CSSIF specimen. Note that the gray data point on the y-axis was obtained from a measurement on the opposite side of the pyramid where material was removed from the non-toolside to a 0.25 mm depth. The stress difference to the purple data point at depth 0 mm, surface at toolside, represents a measure for the disturbance of the stress field from material removal.

6.3. Final strain state

The final von Mises effective strain from experiments at locations 1 through 4 are shown in Fig. 12. Note that the von Mises effective strain in ARGUS is defined by the total, logarithmic, principal strain components and assumes volume constancy:

$$\bar{\varepsilon}_{vM} = \sqrt{\frac{2}{3} \bullet \left(\varepsilon_1^2 + \varepsilon_2^2 + \varepsilon_3^2\right)}, \tag{7}$$

where ε_1, ε_2, and ε_3 are true principal strains. The largest difference in strain between the processes was observed at location 1. TCSSIF had the highest strain, followed by CSSIF, then TSSIF, and, lastly, SPIF with the lowest strain. At location 2, the same order applies although the difference between the processes decreased. At location 3, the strains for the IF processes start to converge, and at location 4, they are nearly equal. This trend with respect to the processes matches that of the force and temperature results with the exception of location 4, which showed higher temperature for SPIF and TSSIF compared to CSSIF and TCSSIF. This is also in agreement with the assumption that the effectiveness of the stress superposition varies throughout the forming process. Based on the trends in Fig. 12, the stress superposition had the greatest effect when the strain increased significantly between locations. Explicitly, the compressive stress superposition appears to be the most effective between locations 1 to 2 (see the largest von Mises strain increase for the CSSIF case), while the tensile stress superposition effect was sustained between locations 1 to 3. As a result, the contributions of each type of stress superposition caused the von Mises strain results for the TCSSIF case. Further analysis into the hierarchy of the forming mechanisms for each process at each location is warranted to improve the understanding of these observations.

To compare the strain values measured from experiments with the FE results, the major and minor strain components were compared directly. The results are shown in Fig. 13. For all four processes, the minor strains are small values, i.e., <0.04, and match well. For SPIF and TSSIF, the FE results slightly overpredicted the major strain values. The increased

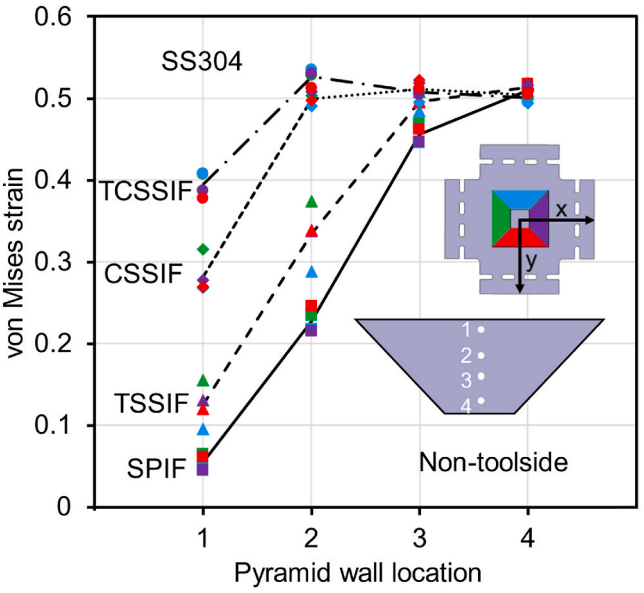

Fig. 12. Von Mises strain at locations 1 through 4 on the non-toolside of truncated square pyramids manufactured by IF processes (exp.). Averages are shown as lines. The strain uncertainty is < 0.005 (1 × σ).

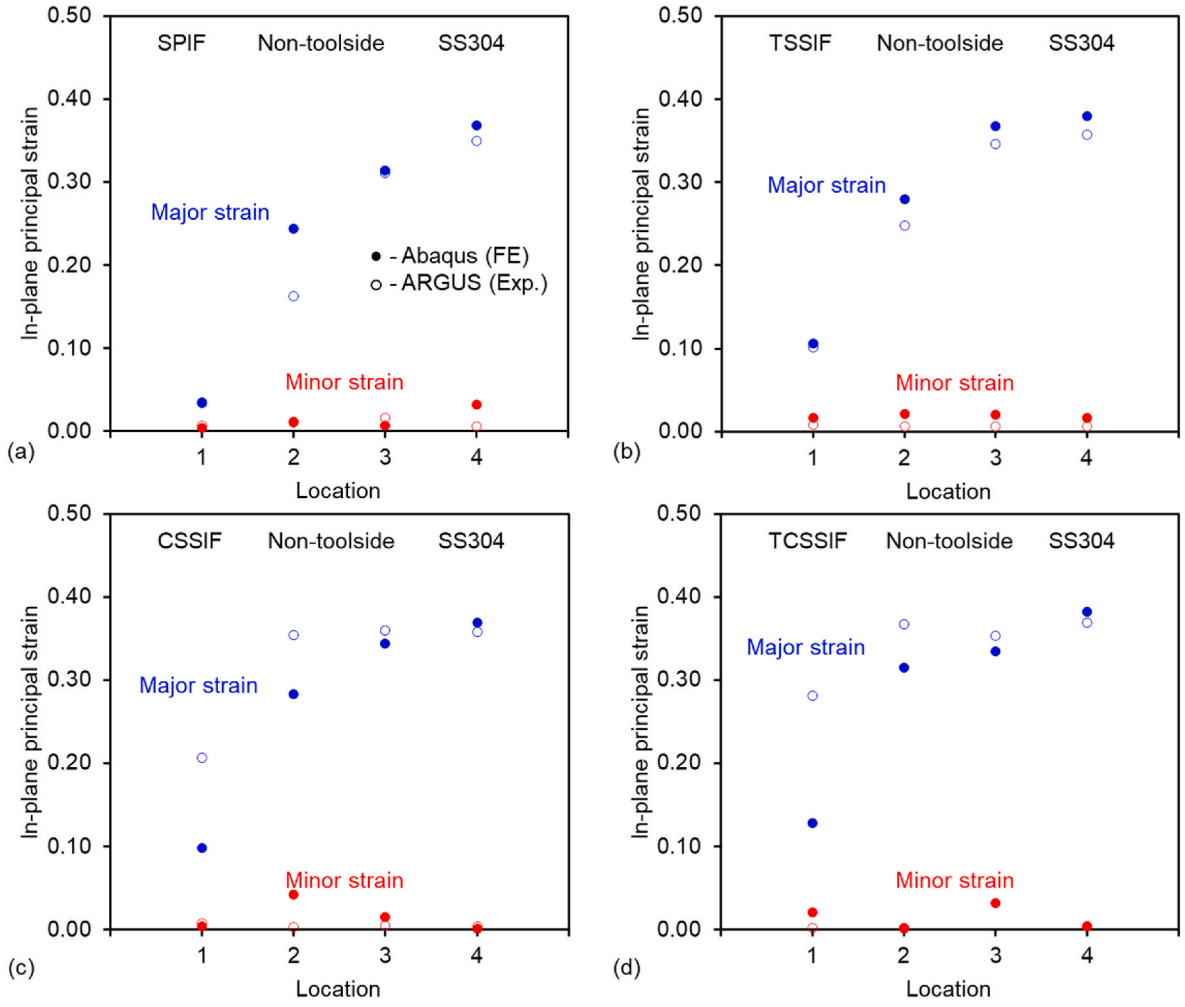

Fig. 13. Comparison of final major and minor in-plane principal strains from experiments and one element simulations for (a) SPIF, (b) TSSIF, (c) CSSIF, and (d) TCSSIF.

strain results are partially caused by the use of a non-deformable tool in the model. For CSSIF and TCSSIF, the same overprediction was expected, but the current results show underpredictions of the major principal strains except for Location 4.

6.4. *Full FE models: stress state and strain evolution*

From the chosen martensitic transformation kinetics model, the stress state can be described by two quantities: the stress triaxiality and Lode angle parameter. Fig. 14 shows the evolution of the stress state throughout the forming process for each IF process with respect to the equivalent plastic strain. These results were extracted from the full model simulations and filtered based on the equivalent plastic strain increment, which represents the effective plastic deformation for the martensite transformation. It should be noted that when the tool is located far away from the element of interest, e.g., on other pyramid walls, a material point (or element in FE simulation) deforms by a very small strain increment, and the associated stress state change does not significantly impact the martensite transformation. Thus, only steps which contained an equivalent plastic strain increase $\Delta\bar{\varepsilon} > 0.001$ are plotted. The largest plastic strain increment values occur when the tool is directly at or near the location of interest.

For all four processes, the Lode angle parameter showed less variation than the stress triaxiality throughout the forming process. At low levels of equivalent plastic strain, i.e., <0.1, the spread of Lode angle parameter values was slightly larger than at higher levels of equivalent plastic strain, where it fluctuated within −0.2 and 0.2. A Lode angle parameter value close to 0 indicates generalized shear, which is expected due to the presence and contact of the tool on this side of the sheet. However, the stress triaxiality (η) showed stronger evolution and different trends for each of the forming processes with respect to equivalent plastic strain. Near location 1, the stress triaxiality parameter was positive for all four processes with values indicative of generalized shear ($\eta = 0$), uniaxial tension ($\eta = 0.33$), plane strain tension ($\eta = 0.58$), and equibiaxial tension ($\eta = 0.67$). For SPIF, near location 3 for high equivalent plastic strain increment data (i.e., >0.6), the stress triaxiality data included negative values, which indicate uniaxial compression ($\eta = -0.33$) and equibiaxial compression ($\eta = -0.67$). For TSSIF, the stress triaxiality remained positive for the majority of the process but included data near zero, i.e., generalized shear ($\eta = 0$), at location 3 and then negative values at location 4, again for high equivalent plastic strain increment data (i.e., >0.6). For CSSIF, the stress triaxiality data has more points at all locations near generalized shear ($\eta = 0$), compared to SPIF and TSSIF, and did not show many negative values, which would indicate compression, at locations 3 and 4. For TCSSIF, again there are more stress triaxiality data points near generalized shear ($\eta = 0$), in particular at location 2, with negative values at location 4 for high equivalent plastic strain increment data (i.e., >0.6).

These differing trends can be attributed to the process variations but also provide information related to the effectiveness of the stress superposition throughout the process. For example, in TSSIF, the stress triaxiality remains positive until location 4 due to the tensile stress

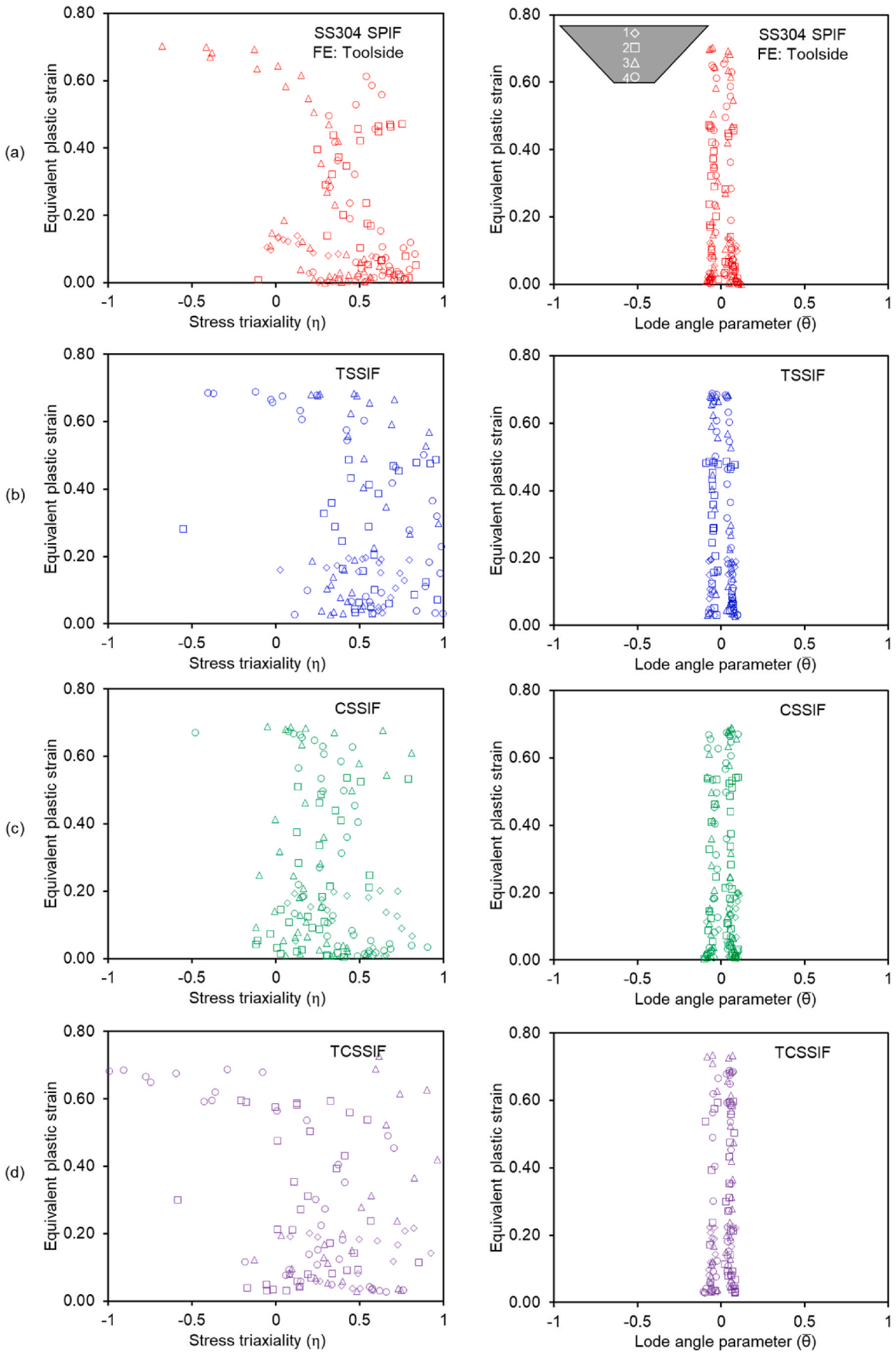

Fig. 14. Stress state evolutions from full FE models of IF processes: toolside stress triaxiality and Lode angle parameter at locations 1 through 4 (shown with different symbols) for (a) SPIF, (b) TSSIF, (c) CSSIF, and (d) TCSSIF.

superposition rather than trending towards negative values at location 3 as is the case in SPIF. This result of stress triaxiality closer to uniaxial tension rather than uniaxial compression resulted in increased phase transformation for TSSIF compared to SPIF (as will be shown in the next section), and is consistent with the martensitic transformation kinetics trend with respect to stress state. For CSSIF, the stress triaxiality is generally closer to zero than SPIF and TSSIF, influenced by the contact between the sheet and the die. For TCSSIF, both tensile and compressive stresses were superposed, and the resulting stress triaxiality appears to be a combination of that shown by SPIF, TSSIF, and CSSIF. The variation in the stress state, particularly the stress triaxiality, for SPIF, TSSIF, CSSIF, and TCSSIF also had significant effects on the phase transformation and is detailed further in the following section.

6.5. Phase transformation

To measure the phase transformation, two methods were used: (1) Feritscope and (2) EBSD. In the first method, the ferrite number was measured on the toolside at four locations along each pyramid wall (as shown in Fig. 3b) by an FMP30 Feritscope (Fischer Technology Inc.). Note that the Feritscope measurement is volumetric and it averages over the entire thickness. The α'-martensite volume fraction was calculated using the preprogrammed conversion factor published by Talonen et al. (2004). The same methodology was repeated to measure the non-toolside at the same locations along each pyramid wall. The Feritscope measurements of the α'-martensite volume fraction, $f_{\alpha'}$, on the toolside and non-toolside are shown in Fig. 15. The measurements on the non-toolside of the truncated square pyramid geometry were consistently lower than the toolside by ~0.1 vol fraction of α'-martensite (same as in [23]) but show the same trends. This observation is consistent with the deformation mechanisms of SPIF, which include increased deformation on the toolside.

Comparing Figs. 12 and 15b, the four processes followed the same trend with respect to one another for all four locations on the non-toolside. TCSSIF had the highest von Mises strain and phase transformation, followed by CSSIF, then TSSIF, and lastly SPIF. Between locations 1 and 2, the von Mises strain and α'-martensite volume fraction increased for all processes except for TCSSIF, which experienced a slight decrease in phase transformation. This is likely the result of the decreasing effectiveness of the tension stress superposition as the forming process progressed, which is reflected in the stress triaxiality evolution towards compression. From location 3 to location 4, the von Mises strain and α'-martensite volume fractions converged for all four processes. Increased von Mises strain leads to increased phase transformation; contrastingly, increased temperature inhibits phase transformation. Since TCSSIF has the largest von Mises strain, temperature increase, and α'-martensite volume fraction at locations 1 and 2, the strain level evidently affects the phase transformation more than the temperature change in the current experiments.

To explain the variation in the Feritscope measurements for the four pyramid walls, two possible explanations are the material anisotropy and the frame in the experimental setup. Since two sides of the frame are fixed and the loading is only applied to the remaining two sides, the loading is not perfectly equibiaxial tension with variations in the biaxial stress state applied on the four sides. Although not considered in this work, anisotropy with respect to martensitic transformation is possible (Beese and Mohr, 2011).

In the second method, EBSD samples were prepared and analyzed for several of the Feritscope measurement locations to validate the α'-martensite volume fraction. Note that EBSD measures a highly localized area in the top layer of grains in comparison to the volumetric measurements of the Feritscope. Additionally, the sample preparation procedure for the EBSD samples is known to influence the phase transformation (Ambrož et al., 2020). The measured value can be artificially increased due to grinding and polishing inducing phase transformation or decreased by removing the surface layer of α'-martensite that was

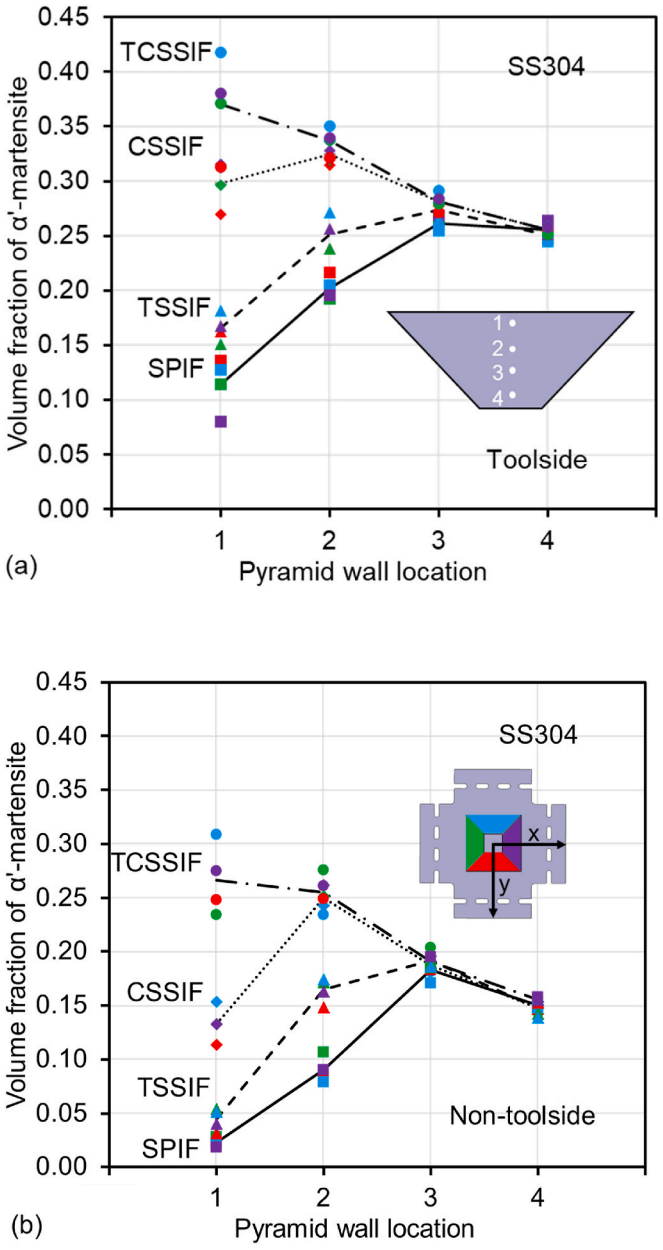

Fig. 15. α'-martensite volume fraction at locations 1–4 on the (a) toolside and (b) non-toolside of truncated square pyramids manufactured by IF processes. Averages of the four pyramid walls are shown as lines. The uncertainty is ±0.005 for volume fractions <0.1, which increases to ±0.015 at volume fractions of 0.3 (1 × σ).

formed on the toolside during incremental forming. A through-thickness gradient of phase transformation results from the incremental forming process are shown in Fig. 16 and in (Mamros et al., 2024). The SEM and EBSD parameters used for these analyses are shown in Table 3.

To validate the Feritscope results, EBSD scans, oriented along the RD-TD plane, were conducted at select locations for the SPIF and TSSIF pyramids. One toolside sample and three non-toolside samples were chosen for analysis. The results are shown in Table 4. Overall, the Feritscope and EBSD results show reasonable agreement, i.e., are within 0.021 α'-martensite of one another, considering the difference in measurement volume mentioned previously. The increased volume fractions in the EBSD measurements compared to the Feritscope measurements are caused by the additional transformation initiated by grinding and polishing.

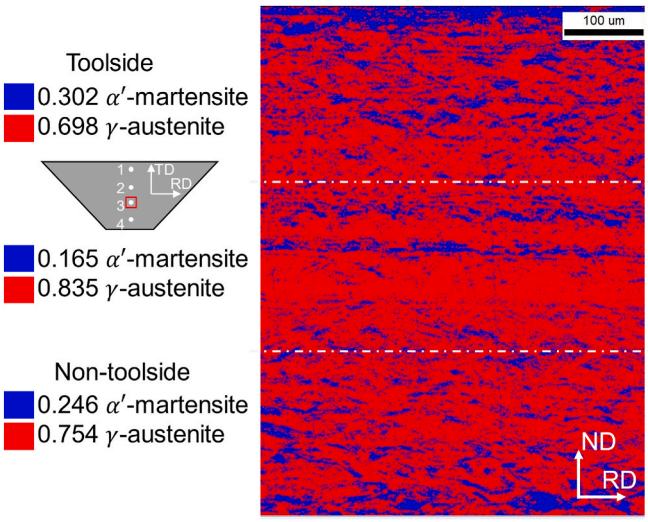

Fig. 16. Volume fraction measurements obtained by EBSD near location 3 along thickness direction of TCSSIF truncated square pyramid sample.

Table 3
SEM and EBSD parameters for phase identification.

Magnification (x)	750
Beam Intensity	19.1
Acceleration Voltage (kV)	20
Sample Tilt (°)	70
Binning	8x8
Step Size (μm)	0.7

Table 4
Comparison of α'-martensite volume fraction measurements by Feritscope and EBSD at the same locations.

Process	Side	Location	α'-martensite volume fraction	
			Feritscope (avg.)	EBSD
SPIF	Non-tool	4	0.158	0.162
SPIF	Tool	3	0.270	0.275
TSSIF	Non-tool	1	0.040	0.061
TSSIF	Non-tool	4	0.252	0.253

Additionally, scans were conducted through the thickness direction, i.e., the RD-ND plane, for a TCSSIF sample to investigate the uniformity of the phase transformation in this plane. Similar to the SPIF sample analyzed in (Mamros et al., 2024), a phase transformation gradient is observed along the thickness direction with a significant α'-martensite layer closest to the toolside surface. However, due to the compressive stress superposition, increased α'-martensite is also observed near the non-toolside compared to SPIF (see Fig. 21 in (Mamros et al., 2024)). The elongated α'-martensite bands observed in the mid-plane were also seen in the same location in the as-received material (Mamros et al., 2024); thus, they were not formed due to the deformation caused by incremental forming. However, the α'-martensite bands may result from the inhomogeneity in the material composition caused by the rolling process (Stauffer et al., 2004). This complex microstructure can lead to certain layers through the thickness of the material that are more susceptible to phase transformation.

The α'-martensite volume fractions predicted by the one element simulations and measured from experiments are shown in Fig. 17. The error bars on the experimental results represent the maximum error, which includes the variation between the four walls of the truncated square pyramids, the repeated Feritscope measurements at each location, and the multiple samples for each process. The EBSD result in Fig. 16 revealed a phase transformation gradient through the thickness of the material. In addition to the toolside and non-toolside predictions, the FE model also provided data related to the midplane of the pyramid walls, which cannot be measured directly using the Feritscope. To better capture this gradient in the simulations, additional elements can be added in the thickness direction with greater computational expense.

In general, the one element simulations provided fair predictions of the α'-martensite volume fractions compared to the experimental values without requiring significant additional computational expense. The implemented martensitic transformation kinetics model is able to capture increasing phase transformation trends with respect to the pyramid wall location well, e.g., SPIF locations 1 through 3. However, in locations where the phase transformation decreases, e.g., from location 1 to location 2 for TCSSIF, a limitation of the model was its inability to capture these downward trends. For locations 1 through 3, the one element simulations underpredicted the phase transformation for all processes, except for SPIF at location 2. This is consistent with the model fitting results for SS304 shown in (Mamros et al., 2024), which show underpredictions for shear and equibiaxial tension stress states. For CSSIF and TCSSIF, in particular, the significant underpredictions of the strain (see Fig. 13) at locations 1 and 2 are consistent with the decreased α'-martensite volume fractions. At location 4, the one element simulations overpredicted the α'-martensite volume fractions due to neglecting the temperature increase during forming that inhibits the phase transformation. In the future, this two-step method could be used with different martensitic transformation kinetics models to improve the predictions, but this optimization is beyond the scope of this present work.

7. Conclusions and future work

The stress superposition of in-plane tensile and normal to the sheet compressive stresses during SPIF to manufacture a truncated square pyramid using SS304 was investigated through experimental and numerical analyses for four IF variants: SPIF, TSSIF, CSSIF, and TCSSIF. Process temperature, axial force, geometry, final strain state, stress state evolution, phase transformation, and residual stress results were analyzed. These results were compared between process variants, measurement methods, and experimental and numerical analyses.

A two-step FE method was utilized to further investigate the phase transformation mechanisms affecting the IF processes. SPIF, TSSIF, CSSIF, and TCSSIF revealed different trends with respect to the stress state evolution during the forming process. Particularly, the stress triaxiality showed greater variation than the Lode angle parameter, which remained close to generalized shear for locations 1 to 4. The different stress state evolutions between the processes affected the phase transformation at each location. However, the α'-martensite volume fraction was ultimately impacted by several effects, including process temperature, equivalent plastic strain level, and stress state, which needed to be considered collectively. A Feritscope was used to measure the α'-martensite volume fraction on the formed truncated square pyramids, and the results were validated by EBSD scans. At locations 1 and 2, TCSSIF had the greatest transformation, followed by CSSIF, then TSSIF, and SPIF had the least amount of transformation. At locations 3 and 4, the four processes converged to similar volume fractions of α'-martensite as well as strain values and forming force. The geometrical accuracy, which was impacted by the residual stresses and springback, revealed the same trend as the martensitic transformation, i.e., TCSSIF had the closest geometry to the target. Further investigations are planned to establish a better understanding of the relationship between the martensitic transformation and residual stress development in SS304 during SSIF. For example, energy analyses of the numerical results, following the procedure described in (Maaβ et al., 2019; Maqbool and Bambach, 2018), may provide insight regarding the contributions of each deformation mechanism at different locations on the pyramid wall and for different incremental forming processes. However, the current

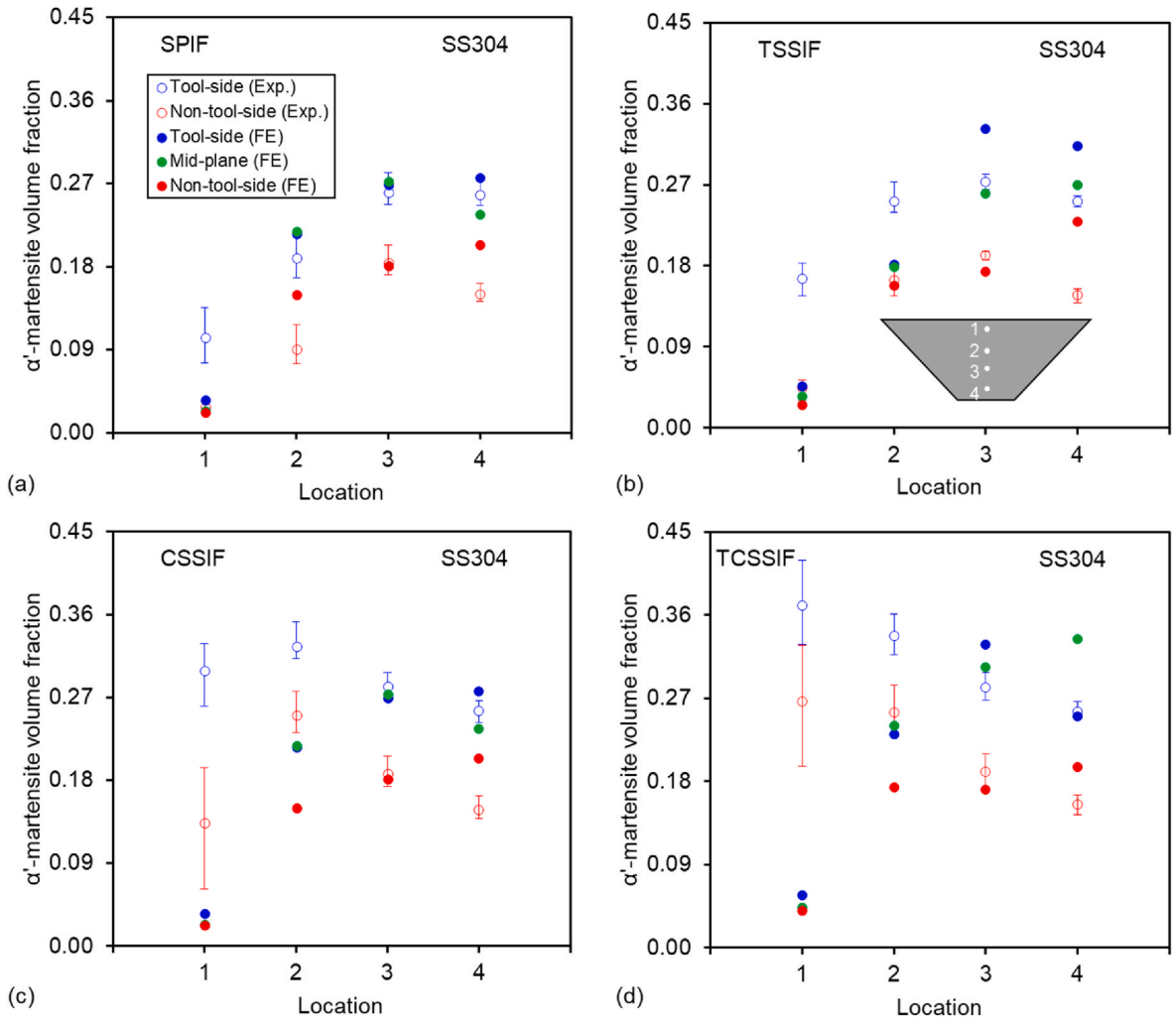

Fig. 17. Comparison of α'-martensite volume fraction measurements from Feritscope (Exp.) with predictions from one element simulations (FE). Error bars indicate maximum and minimum measurements.

results support that functionally graded, formed parts can be created from these manufacturing processes for implementation into several industries. For example, biomedical trauma fixation hardware requires patient-specific geometries and heterogeneous material properties, e.g., increased strength near the fixture locations of an implant.

In addition to deriving toolpath strategies based on stress superposition from these results, process modifications can be used simultaneously to assist with manipulating the phase transformation during forming. To increase the tensile stress superposition effect, a thinner sheet could be used or a frame with an increased maximum capacity could be built. Alternatively, a stretch forming setup could potentially replace the current frame design for easy implementation into an existing industrial setup (Choi and Lee, 2019). For all IF processes, temperature control could be introduced to locally affect the temperature and thus martensite transformation, e.g., by using vortex tubes mounted to the tool spindle as in (Darzi et al., 2023).

CRediT authorship contribution statement

Elizabeth M. Mamros: Writing – review & editing, Writing – original draft, Visualization, Validation, Software, Project administration, Methodology, Investigation, Funding acquisition, Formal analysis, Data curation, Conceptualization. **Fabian Maaß:** Writing – review & editing, Writing – original draft, Software, Resources, Methodology, Investigation, Conceptualization. **Thomas H. Gnäupel-Herold:** Writing – review & editing, Writing – original draft, Resources, Methodology, Investigation, Formal analysis, Data curation. **A. Erman Tekkaya:** Writing – review & editing, Supervision, Resources, Methodology, Conceptualization. **Brad L. Kinsey:** Writing – review & editing, Supervision, Methodology, Funding acquisition, Conceptualization. **Jinjin Ha:** Writing – review & editing, Supervision, Software, Methodology, Funding acquisition, Conceptualization.

Disclaimer

Certain commercial suppliers or materials are identified in this paper to foster understanding. Such identification does not imply recommendation or endorsement by the National Institute of Standards and Technology, nor does it imply that the materials or equipment identified are necessarily the best available for the purpose.

Declaration of competing interest

The authors declare that they have no known competing financial interests or personal relationships that could have appeared to influence the work reported in this paper.

Acknowledgements

Support for the New Hampshire Center for Multiscale Modeling and

Manufacturing of Biomaterials (NH BioMade) project was provided by the US National Science Foundation (NSF) EPSCoR award (#1757371). This research was also supported by the Institute of International Education Graduate International Research Experiences program (NSF #1829436), the German-American Fulbright Commission, and the Germanistic Society of America.

The authors would like to thank Dr. Marlon Hahn (IUL), Dr. Adam Creuziger (NIST), and Dr. Mark Iadicola (NIST) for insightful discussions. The authors would also like to thank Dirk Hoffman for assisting with the specimen and die preparation at IUL and Nancy Cherim and Sarah Mayer for their assistance with the EBSD scans. The SEM/FIB used is managed by the University of New Hampshire's (UNH's) University Instrumentation Center (UIC) and was purchased with funds awarded to UNH from the US National Science Foundation (NSF) (MRI Grant 1337897) with additional funds from UNH. EDS/EBSD components on this system were purchased with start-up funds from UNH at the discretion of Professor Marko Knezevic.

Data availability

Data will be made available on request.

References

Ambrož, O., Mikmeková, Š., Hegrová, V., Aoyama, T., 2020. TRIP steel specimen preparation for advanced SEM and EBSD. Presented at the METAL 2020, 518–522. https://doi.org/10.37904/metal.2020.3513.

ASTM International, 2024. Standard test methods for tension testing of metallic materials. https://doi.org/10.1520/E0008_E0008M-24.

Becker, C., Tekkaya, A.E., Kleiner, M., 2014. Fundamentals of the incremental tube forming process. CIRP Ann. 63, 253.

Beese, A.M., Mohr, D., 2011. Effect of stress triaxiality and Lode angle on the kinetics of strain-induced austenite-to-martensite transformation. Acta Mater. 59, 2589–2600. https://doi.org/10.1016/j.actamat.2010.12.040.

Bochniak, W., Korbel, A., 2003. KOBO Type Forming: forging of metals under complex conditions of the process. J. Mater. Process. Technol. 134, 120–134. https://doi.org/10.1016/S0924-0136(02)01033-6.

Bochniak, W., Korbel, A., 2000. Plastic flow of aluminium extruded under complex conditions. Mater. Sci. Technol. 16, 664–669. https://doi.org/10.1179/026708300101508243.

Bochniak, W., Marszowski, K., Korbel, A., 2005. Theoretical and practical aspects of the production of thin-walled tubes by the KOBO method. J. Mater. Process. Technol. 169, 44–53. https://doi.org/10.1016/j.jmatprotec.2005.02.258.

Castrol Iloform PN 226 Datasheet, 2008.

Cheng, Z., Li, Y., Xu, C., Liu, Y., Ghafoor, S., Li, F., 2020. Incremental sheet forming towards biomedical implants: a review. J. Mater. Res. Technol. 9, 7225–7251. https://doi.org/10.1016/j.jmrt.2020.04.096.

Choi, H., Lee, C., 2019. A mathematical model to predict thickness distribution and formability of incremental forming combined with stretch forming. Robotics and Computer-Integrated Manufacturing, Extended Papers Selected from FAIM2016 55, 164–172. https://doi.org/10.1016/j.rcim.2018.07.014.

Darzi, S., Adams, M.D., Roth, J.T., Kinsey, B.L., Ha, J., 2023. Manipulating martensite transformation of SS304L during double-sided incremental forming by varying temperature and deformation path. CIRP Ann. - Manuf. Technol.

Darzi, S., Kinsey, B., Ha, J., 2024a. Reforming toolpath effect on deformation mechanics in double-sided incremental forming. Int. J. Mech. Sci. https://doi.org/10.1016/j.ijmecsci.2024.109548.

Darzi, S., Tulung, E., Kinsey, B.L., Ha, J., 2024b. Localized manipulation of martensite transformation in double-sided incremental forming by varying the deformation path. J. Manuf. Sci. Eng. 146. https://doi.org/10.1115/1.4066123.

Data Sheet for the Probes FGAB1.3-Fe and EGAB1.3-Fe, n.d..

DIN 51524-2, 2017. Pressure Fluids - Hydraulic Oils - Part 2: HLP Hydraulic Oils, Minimum Requirements. European Standards.

Dingley, D., 2004. Progressive steps in the development of electron backscatter diffraction and orientation imaging microscopy. J. Microsc. 213, 214–224. https://doi.org/10.1111/j.0022-2720.2004.01321.x.

Duflou, J.R., Habraken, A.-M., Cao, J., Malhotra, R., Bambach, M., Adams, D., Vanhove, H., Mohammadi, A., Jeswiet, J., 2018. Single point incremental forming: state-of-the-art and prospects. Int. J. Material Form. 11, 743–773. https://doi.org/10.1007/s12289-017-1387-y.

Emmens, W.C., van den Boogaard, A.H., 2009. Incremental forming by continuous bending under tension—an experimental investigation. J. Mater. Process. Technol. 209, 5456–5463. https://doi.org/10.1016/j.jmatprotec.2009.04.023.

Fatemi, A., Mollaei Dariani, B., 2024. Hydro-assisted incremental forming (HAIF): a formability-enhanced incremental forming process; presenting an experimental method for determination of forming limits with generalized non-planar stress state. Adv. Ind. Manuf. Eng. 9, 100143. https://doi.org/10.1016/j.aime.2024.100143.

Feng, Z., Mamros, E.M., Ha, J., Kinsey, B.L., Knezevic, M., 2021. Modeling of plasticity-induced martensitic transformation to achieve hierarchical, heterogeneous, and tailored microstructures in stainless steels. CIRP J. Manuf. Sci. Technol 33, 389–397. https://doi.org/10.1016/j.cirpj.2021.04.006.

Gnäupel-Herold, T., 2023. Elastic behaviour of orientation-correlated grains in multiphase aggregates. J. Appl. Crystallogr. 56, 1658–1673. https://doi.org/10.1107/S1600576723008312.

Gnaupel-Herold, T., 2022. IsoDEC Download.

Ha, J., Mayer, S., Feng, Z., Matukhno, N., Knezevic, M., Kinsey, B.L., 2022. Inducing texture in AA5182-O through continuous-bending-under-tension and recovery heat treatment processes to influence r-values. CIRP Ann. https://doi.org/10.1016/j.cirp.2022.04.059.

Hibbitt, D., Karlsson, B., Sorensen, P., 1978. Abaqus.

ISO 6892-1:2019, 2019. Metallic Materials — Tensile Testing — Part 1: Method of Test at Room Temperature.

ISO 7743:2017, 2017. Rubber, Vulcanized or Thermoplastic — Determination of Compression Stress-Strain Properties. ISO.

Jiang, Z., Ehmann, K.F., Cao, J., 2022. Prediction of forming temperature in electrically-assisted double-sided incremental forming using a neural network. J. Mater. Process. Technol. 302, 117486. https://doi.org/10.1016/j.jmatprotec.2021.117486.

Kalpakjian, S., Schmid, S., 2013. Manufacturing Engineering and Technology, seventh ed. Pearson Education.

Katajarinne, T., Louhenkilpi, S., Kivivuori, S., 2014. A novel approach to control the properties of austenitic stainless steels in incremental forming. Mater. Sci. Eng., A 604, 23–26. https://doi.org/10.1016/j.msea.2014.03.020.

Korbel, A., Bochniak, W., 2004. Refinement and control of the metal structure elements by plastic deformation. Scr. Mater. - SCRIPTA MATER. 51, 755–759. https://doi.org/10.1016/j.scriptamat.2004.06.020.

Lu, B., Ou, H., Shi, S.Q., Long, H., Chen, J., 2016. Titanium based cranial reconstruction using incremental sheet forming. Int. J. Material Form. 9, 361–370. https://doi.org/10.1007/s12289-014-1205-8.

Luo, C., Yuan, H., 2022. Measurement and modeling of deformation-induced martensitic transformation in a metastable austenitic stainless steel under cyclic loadings. Acta Mater. 238, 118202. https://doi.org/10.1016/j.actamat.2022.118202.

Maaß, F., Hahn, M., Tekkaya, A.E., 2022. Setting residual stresses in tensile stress-superposed incremental sheet forming. In: Proceedings of the 22nd International Conference on Material Forming. Presented at the ESAFORM 2022.

Maaß, F., Hahn, M., Tekkaya, A.E., 2021. Adjusting residual stresses by flexible stress superposition in incremental sheet metal forming. Arch. Appl. Mech. 91, 3489–3499. https://doi.org/10.1007/s00419-021-01929-x.

Maaß, F., Hahn, M., Tekkaya, A.E., 2020a. Interaction of process parameters, forming mechanisms, and residual stresses in single point incremental forming. Metals 10, 656. https://doi.org/10.3390/met10050656.

Maaß, F., Hahn, M., Tekkaya, A.E., 2020b. Interaction of process parameters, forming mechanisms, and residual stresses in single point incremental forming. Metals 10, 656. https://doi.org/10.3390/met10050656.

Maaß, F., Hahn, M., Tekkaya, A.E., Dobecki, M., Poeche, A., Brömmelhoff, K., Reimers, W., 2019. Forming mechanisms-related residual stress development in single point incremental forming. Prod. Eng. Res. Dev. 13, 149–156. https://doi.org/10.1007/s11740-018-0867-3.

Mamros, E.M., Maaß, F., Hahn, M., Tekkaya, A.E., Ha, J., Kinsey, B.L., 2022. Superposing tensile stresses into single point incremental forming to affect martensitic transformation of SS304. IOP Conf. Ser. Mater. Sci. Eng. 1238, 012085. https://doi.org/10.1088/1757-899X/1238/1/012085.

Mamros, E.M., Maaß, F., Tekkaya, A.E., Kinsey, B.L., Ha, J., 2024. Martensitic transformation of SS304 truncated square pyramid manufactured by single point incremental forming. CIRP J. Manuf. Sci. Technol 55, 28–41. https://doi.org/10.1016/j.cirpj.2024.08.006.

Mamros, E.M., Polec, L.A., Maaß, F., Clausmeyer, T., Tekkaya, A.E., Ha, J., Kinsey, B.L., 2023. Examination of bending stress superposition effect on martensite transformation in austenitic stainless steel 304. In: Presented at the International Conference on the Technology of Plasticity, France. https://doi.org/10.1007/978-3-031-40920-2_49.

Maqbool, F., Bambach, M., 2018. Dominant deformation mechanisms in single point incremental forming (SPIF) and their effect on geometrical accuracy. Int. J. Mech. Sci. 136, 279–292. https://doi.org/10.1016/j.ijmecsci.2017.12.053.

Martins, P.A.F., Bay, N., Skjoedt, M., Silva, M.B., 2008. Theory of single point incremental forming. CIRP Ann. 57, 247–252. https://doi.org/10.1016/j.cirp.2008.03.047.

Mayer, S., Matukhno, N., Kinsey, B.L., Knezevic, M., Ha, J., 2024. Manipulation of strength and ductility of AA5182-O through cyclic bending under tension and annealing processing. J. Manuf. Process. 124, 673–688. https://doi.org/10.1016/j.jmapro.2024.06.042.

Mooney, M., 1940. A theory of large elastic deformation. J. Appl. Phys. 11, 582–592. https://doi.org/10.1063/1.1712836.

Moser, N., 2019. Deformation Mechanisms and Process Planning in Double-Sided Incremental Forming.

Moser, N., Leem, D., Ehmann, K., Cao, J., 2021. A high-fidelity simulation of double-sided incremental forming: improving the accuracy by incorporating the effects of machine compliance. J. Mater. Process. Technol. 295, 117152.

Olson, G., Cohen, M., 1975. Kinetics of strain-induced martensitic nucleation. Metall. Trans. A 6, 791–795. https://doi.org/10.1007/BF02672301.

Peng, W., Ou, H., 2023. Deformation mechanisms and fracture in tension under cyclic bending plus compression, single point and double-sided incremental sheet forming processes. I. J. Mach. Tools. 184, 103980. https://doi.org/10.1016/j.ijmachtools.2022.103980.

Pompe, W., Worch, H., Epple, M., Friess, W., Gelinsky, M., Greil, P., Hempel, U., Scharnweber, D., Schulte, K., 2003. Functionally graded materials for biomedical

applications. Mater. Sci. Eng.: A, Papers from the German Priority Programme (Functionally Graded Materials) 362, 40–60. https://doi.org/10.1016/S0921-5093(03)00580-X.

Poulin, C.M., Vogel, S.C., Korkolis, Y.P., Kinsey, B.L., Knezevic, M., 2020. Experimental studies into the role of cyclic bending during stretching of dual-phase steel sheets. Int. J. Material Form. 13, 393–408. https://doi.org/10.1007/s12289-019-01530-2.

Santacreu, P.-O., Glez, J.-C., Chinouilh, G., Fröhlich, T., 2006. Behaviour model of austenitic stainless steels for automotive structural parts. Steel Res. Int. 77, 686–691. https://doi.org/10.1002/srin.200606448.

Stauffer, A.C., Koss, D.A., McKirgan, J.B., 2004. Microstructural banding and failure of a stainless steel. Metall. Mater. Trans. A 35, 1317–1324. https://doi.org/10.1007/s11661-004-0306-2.

Stommel, M., Stojek, M., Korte, W., 2018. Mechanisches Werkstoffverhalten und -modellierung. In: FEM Zur Berechnung von Kunststoff- Und Elastomerbauteilen. Carl Hanser Verlag GmbH & Co. KG, pp. 5–144. https://doi.org/10.3139/9783446452831.002.

Stringfellow, R.G., Parks, D.M., Olson, G.B., 1992. A constitutive model for transformation plasticity accompanying strain-induced martensitic transformations in metastable austenitic steels. Acta Metall. Mater. 40, 1703–1716. https://doi.org/10.1016/0956-7151(92)90114-T.

Talonen, J., Aspegren, P., Hänninen, H., 2004. Comparison of different methods for measuring strain induced martensite content in austenitic steels. Mater. Sci. Technol. 20, 1506–1512. https://doi.org/10.1179/026708304X4367.

Tekkaya, A.E., Groche, P., Kinsey, B., Wang, Z.G., 2023. Stress superposition in metal forming. CIRP Ann. https://doi.org/10.1016/j.cirp.2023.04.090.

Timoshenko, S., Woinowsky-Krieger, S., 1959. Theory of Plates and Shells. McGraw-Hill.